9

Polarized Light Assessment of Complex Turbid Media Such as Biological Tissues Using Mueller Matrix Decomposition

Nirmalya Ghosh

IISER Kolkata, Mohanpur Campus, PO: BCKV Campus Main Office, Mohanpur 741252, West Bengal, India

Michael Wood, and Alex Vitkin

Ontario Cancer Institute / Department of Medical Biophysics University of Toronto, Toronto, Ontario, Canada

Polarization parameters of light scattered from biological tissue contain rich morphological and functional information of potential biomedical importance. Despite the wealth of interesting parameters that can be probed with polarized light, in optically thick turbid media such as tissues, numerous complexities due to multiple scattering and simultaneous occurrence of many polarization effects present formidable challenges, both in terms of accurate measurement and in terms of extraction/unique interpretation of the polarization parameters. In this chapter, we describe the application of an expanded Mueller matrix decomposition method to tackle these complexities. The ability of this approach to delineate individual intrinsic polarimetry characteristics in tissue-like turbid media (exhibiting multiple scattering, and linear and circular birefringence) was validated theoretically with a polarized-light propagation model and experimentally with a polarization-modulation/synchronous detection technique. The details of the experimental turbid polarime-

try system, forward Monte Carlo modeling, inverse polar decomposition analysis, and the results of the validations studies are presented in this chapter. Initial applications of this promising approach in two scenarios of significant clinical interest, that for monitoring regenerative treatments of the heart and for noninvasive glucose measurements, as well as initial *in vivo* demonstration, are discussed.

Key words: polarization, multiple scattering, turbid polarimetry, light transport, Monte Carlo simulations, Stokes vector, Mueller matrix, polar decomposition, biological and medical applications

9.1 Introduction

Polarimetry has played important roles in our understanding of the nature of electromagnetic waves, elucidating the three-dimensional characteristics of chemical bonds, uncovering the asymmetric (chiral) nature of many biological molecules, quantifying protein properties in solutions, supplying a variety of nondestructive evaluation methods, and contributing to remote sensing in meteorology and astronomy [1–3]. The use of polarimetric approaches has also received considerable recent attention in biophotonics [4–6]. This is because polarization parameters of light scattered from biological tissue contain rich morphological and functional information of potential biomedical importance. For example, the anisotropic organized nature of many tissues stemming from their fibrous structure leads to linear birefringence (or linear retardance), manifest as anisotropic refractive indices parallel and perpendicular to the fibers. Muscle fibers and extracellular matrix proteins (such as collagen and elastin) possess this fibrous structure and accordingly exhibit linear birefringence. Changes in this anisotropy resulting from disease progression or treatment response alter the optical birefringence properties, making this a potentially sensitive probe of tissue status [7,8]. Glucose, another important tissue constituent, exhibits circular birefringence due to its asymmetric chiral structure. Its presence in tissue leads to rotation of the plane of linearly polarized light about the axis of propagation (known as optical rotation or optical activity). Measurements of optical rotation may offer an attractive approach for noninvasive monitoring of tissue glucose levels [9–14].

Despite the wealth of interesting properties that can be probed with polarized light, in optically thick turbid media such as tissues, numerous complexities due to multiple scattering present formidable challenges. Multiple scattering causes extensive depolarization that confounds the established techniques. Further, even if some residual polarization signal can be measured, multiple scattering also alters the polarization state, for example by scattering-induced diattenuation and by scattering-induced changes in the orientation of the linear polarization vector that appears as optical rotation [10,14]. Quantitative polarimetry in tissue is further compromised by simultaneous occurrences of many polarization effects.

The Mueller matrix represents the transfer function of an optical system in its interactions with polarized light, the elements reflecting various sample properties of potential interest [15, 16]. However, in complex turbid media such as tissues, many optical polarization effects occur simultaneously (the most common biopolarimetry events are depolarization, linear birefringence, and optical activity), and contribute in a complex interrelated way to the Mueller matrix elements. Hence, these represent several "lumped" effects, masking potentially interesting ones and hindering unique data interpretation. The challenges are thus to minimize or compensate for multiple scattering, and to decouple the individual contributions of simultaneously occurring polarization effects. Each of the individual processes, if separately extracted from the "lumped" system Mueller matrix, can potentially be used as a useful biological metric.

We have recently developed and validated an expanded Mueller matrix decomposition approach for extraction, quantification and unique interpretation of individual intrinsic polarimetry characteristics in complex tissue-like turbid media [17,18]. The ability of this approach to delineate individual intrinsic polarimetry characteristics was validated theoretically with a polarized-light propagation model, and experimentally with a polarization-modulation/synchronous detection technique. In this chapter, we summarize this (and related) research on turbid polarimetry, and discuss initial biomedical applications of this promising approach.

This chapter is organized as follows. In section 9.2, we describe the basics of Mueller matrix algebra and also define the constituent polarization parameters. The mathematical methodology of polar decomposition for extraction of the individual intrinsic polarimetry characteristics from "lumped" Mueller matrix is outlined in section 9.3. Section 9.4 describes the high-sensitivity polarization modulation / synchronous detection experimental system capable of measuring complete Mueller matrix elements from strongly depolarizing scattering media such as tissues. This is followed by the description of the corresponding theoretical model in section 9.5, based on the forward Monte Carlo (MC) modeling, with the flexibility to incorporate all the simultaneous optical (scattering and polarization) effects. Section 9.6 reviews the experimental and theoretical validation results of the polar decomposition approach to delineate individual intrinsic polarimetry characteristics in complex tissue-like turbid media. In section 9.7, we present selected trends of the dependence of decomposition-derived polarization parameters on multiple scattering, propagation path, and detection geometry. In section 9.8, we discuss the initial applications of the Mueller matrix decomposition approach in two scenarios of significant clinical interest, for noninvasive glucose measurements and for monitoring of regenerative treatments of the heart. The proof-of-principle demonstration of *in vivo* use of this method for polarization-based characterization of tissue is also presented in this section. The chapter concludes with a discussion of the prospective biomedical utility of this promising approach.

9.2 Mueller Matrix Preliminaries and the Basic Polarization Parameters

The state of polarization of a beam of light can be represented by four measurable quantities (known as Stokes parameters) that, when grouped in a 4×1 vector, are known as the Stokes vector [15], introduced by G. G. Stokes in 1852. The four Stokes parameters are defined relative to the following six intensity measurements (I) performed with ideal polarizers: I_H, horizontal linear polarizer (0°); I_V, vertical linear polarizer (90°); I_P, 45° linear polarizer; I_M, 135° (-45°) linear polarizer; I_R, right circular polarizer, and I_L, left circular polarizer. The Stokes vector (**S**) is defined as

$$\mathbf{S} = \begin{bmatrix} I \\ Q \\ U \\ V \end{bmatrix} = \begin{bmatrix} IH + IV \\ IH - IV \\ IP - IM \\ IR - IL \end{bmatrix} \tag{9.1}$$

where I, Q, U, and V are Stokes vector elements. I is the total detected light intensity that corresponds to addition of any two orthogonal component intensities, while Q is the portion of the intensity that corresponds to the difference between horizontal and vertical polarization states, U is the portion of the intensity that corresponds to the difference between intensities of linear $+45^\circ$ and -45° polarization states, and V is portion of the intensity that corresponds to the difference between intensities of right circular and left circular polarization states. For a completely polarized beam of

light, the Stokes parameters are not all independent [15]

$$I = \sqrt{Q^2 + U^2 + V^2}. \tag{9.2}$$

From Stokes vector elements, the following polarization parameters of partially polarized light can be determined [15]:
degree of polarization

$$DOP = \sqrt{Q^2 + U^2 + V^2}/I, \tag{9.3}$$

degree of linear polarization

$$DOLP = \frac{\sqrt{Q^2 + U^2}}{I}, \tag{9.4}$$

and degree of circular polarization

$$DOCP = \frac{V}{I}. \tag{9.5}$$

While the Stokes vector represents the polarization properties of the *light*, the Mueller matrix (**M**) contains complete information about all the polarization properties of the *medium*. The Mueller matrix **M** (a 4×4 matrix) is a mathematical description of how an optical sample interacts or transforms the polarization state of an incident light beam. In essence, the Muller matrix can be thought of as the "optical fingerprint" or transfer function of a sample. Mathematically, this matrix operates directly on an input or incident Stokes vector, resulting in an output Stokes vector that describes the polarization state of the light leaving the sample. This is described mathematically by the following equation:

$$\mathbf{S}_o = \mathbf{M} \cdot \mathbf{S}_i. \tag{9.6}$$

$$\begin{bmatrix} I_o \\ Q_o \\ U_o \\ V_o \end{bmatrix} = \begin{bmatrix} m_{11} & m_{12} & m_{13} & m_{14} \\ m_{21} & m_{22} & m_{23} & m_{24} \\ m_{31} & m_{32} & m_{33} & m_{34} \\ m_{41} & m_{42} & m_{43} & m_{44} \end{bmatrix} \begin{bmatrix} I_i \\ Q_i \\ U_i \\ V_i \end{bmatrix} = \begin{bmatrix} m_{11}I_i + m_{12}Q_i + m_{13}U_i + m_{14}V_i \\ m_{21}I_i + m_{22}Q_i + m_{23}U_i + m_{24}V \\ m_{31}I_i + m_{32}Q_i + m_{33}U_i + m_{34}V \\ m_{41}I_i + m_{42}Q_i + m_{43}U_i + m_{44}V \end{bmatrix}, \tag{9.7}$$

where $\mathbf{S}_o$ and $\mathbf{S}_i$ are the output and input Stokes vectors, respectively.

The different polarization properties of a medium are coded in the various elements of the Mueller matrix **M**. The three basic polarization properties are diattenuation (differential attenuation of orthogonal polarization), retardance (de-phasing of orthogonal polarization) and depolarization; the functional forms of the corresponding matrices are well known [15].

Diattenuation

Diattenuation (d) by an optical element corresponds to differential attenuation of orthogonal polarizations for both linear and circular polarization states. Accordingly, linear diattenuation is defined as differential attenuation of two orthogonal linear polarization states and circular diattenuation is defined as differential attenuation of right circular polarized light (RCP) and left circular polarized light (LCP). Mathematically, the Mueller matrix for an ideal diattenuator can be defined using two intensity measurements, q and r,for the two incident orthogonal polarization states (either linear or circular). Using this convention, the general Mueller matrix for a linear diattenuator is defined as

$$\begin{pmatrix} q+r & (q-r)\cos 2\theta & (q-r)\sin 2\theta & 0 \\ (q-r)\cos 2\theta & (q+r)\cos^2 2\theta + 2\sqrt{(qr)}\sin^2 2\theta & \left(q+r-2\sqrt{(qr)}\right)\sin 2\theta \cos 2\theta & 0 \\ (q-r)\sin 2\theta & \left(q+r-2\sqrt{(qr)}\right)\sin 2\theta \cos 2\theta & (q+r)\cos^2 2\theta + 2\sqrt{(qr)}\sin^2 2\theta & 0 \\ 0 & 0 & 0 & 2\sqrt{(qr)} \end{pmatrix}. \tag{9.8}$$

where θ is the angle between the diattenuation axis of the sample and the horizontal (laboratory) frame. Briefly, the sample's diattenuation axis is the direction of minimum attenuation (an analogous definition exits for sample's birefringence axis, as detailed further in the next section). Similarly for circular diattenuation, the general form of Mueller matrix is

$$\begin{pmatrix} q+r & 0 & 0 & q-r \\ 0 & 2\sqrt{(qr)} & 0 & 0 \\ 0 & 0 & 2\sqrt{(qr)} & 0 \\ q-r & 0 & 0 & q+r \end{pmatrix}. \tag{9.9}$$

Ideal polarizers that transform incident unpolarized light to completely polarized light are examples of diattenuators (with magnitude of diattenuation $d = 1.0$ for ideal polarizer; d is a dimensionless quantity, ranging from 0 to 1.0). Note that this is analogous to dichroism, which is defined as the differential absorption of two orthogonal linear polarization states (linear dichroism) or of CP states (circular dichroism). The term "diattenuation" is more general in that it is defined in terms of differential attenuation (either by absorption or scattering). Many biological molecules (such as amino acids, proteins, nucleic acids) exhibit dichroism or diattenuation effects.

Retardance

Retardance is the de-phasing of the two orthogonal polarization states. Linear retardance (δ) arises due to difference in phase between orthogonal linear polarization states (between vertical and horizontal or between 45° and -45°). Circular retardance or optical rotation (ψ) arises due to difference in phase between RCP and LCP.

The general form of a Mueller matrix of a linear retarder with retardance δ and orientation angle of retarder axis θ is [15]

$$\begin{pmatrix} 1 & 0 & 0 & 0 \\ 0 & \cos^2 2\theta + \sin^2 2\theta \cos\delta & \sin 2\theta \cos 2\theta (1-\cos\delta) & -\sin 2\theta \sin\delta \\ 0 & \sin 2\theta \cos 2\theta (1-\cos\delta) & \sin^2 2\theta + \cos^2 2\theta \cos\delta & \cos 2\theta \sin\delta \\ 0 & \sin 2\theta \sin\delta & -\cos 2\theta \sin\delta & \cos\delta \end{pmatrix}. \tag{9.10}$$

where θ is the angle between the retardation axis of the sample and the horizontal (laboratory) frame. Similarly, the Mueller matrix for a circular retarder with retardance ψ is

$$\begin{pmatrix} 1 & 0 & 0 & 0 \\ 0 & \cos 2\psi & -\sin 2\psi & 0 \\ 0 & \sin 2\psi & \cos 2\psi & 0 \\ 0 & 0 & 0 & 1 \end{pmatrix}. \tag{9.11}$$

Linear retardance has its origin in anisotropy in refractive indices, which leads to phase retardation between two orthogonal linear polarization states. In tissue, muscle fibers and extracellular matrix proteins (such as collagen and elastin) possess such anisotropy and thus exhibit linear birefringence. Circular retardance or optical rotation arises due to asymmetric chiral structures. In tissue, glucose and other constituents such as proteins and lipids possess such chiral structure and accordingly exhibit circular retardance. Note that while diattenuation is associated with amplitude difference in the two orthogonal field components (either for linearly or circularly polarized field), retardance is associated with phase difference between orthogonal field components.

Depolarization

If an incident state is polarized and the exiting state has a degree of polarization less than one, then the sample exhibits depolarization. Depolarization is intrinsically associated with scattering, resulting in losses of directionality, phase, and coherence of the incident polarized beam. In a turbid medium like biological tissue, multiple scattering is the major source of depolarization. The general form of the depolarization Mueller matrix is

$$M_\Delta = \begin{pmatrix} 1 & 0 & 0 & 0 \\ 0 & a & 0 & 0 \\ 0 & 0 & b & 0 \\ 0 & 0 & 0 & c \end{pmatrix}, \qquad |a|, |b|, |c| \leq 1. \tag{9.12}$$

Here $1-|a|$ and $1-|b|$ are depolarization factors for linear polarization, and $1-|c|$ is the depolarization factor for circular polarization. Note that this definition of depolarization factor is different from the Stokes parameter-based definition of degrees of polarization [Eqs. (9.3)–(9.5)]. The latter represents the value of degree of polarization of the emerging beam, and result from several lumped polarization interactions. In contrast, the depolarization factors of Eq. (9.12) represent the pure depolarizing transfer function of the medium.

The operational definition of the Mueller matrices of the polarization properties, described above, enables one to correctly forward model these individual effects of any medium. However, the problem arises when all these polarization effects are exhibited simultaneously in a medium [as is the case for biological tissue that often exhibit depolarization, linear birefringence, optical activity, and diattenuation (the magnitude of diattenuation in tissue is, however, much lower compared to the other effects)]. Simultaneous occurrence of many polarization effects contributes in a complex interrelated way to the resulting Mueller matrix elements. Hence, these represent several "lumped" effects, hindering their extraction / unique interpretation and necessitating additional analysis to decouple the individual sample characteristics. In the following section, we describe a matrix decomposition method to tackle this problem.

9.3 Polar Decomposition of Mueller Matrices for Extraction of the Individual Intrinsic Polarization Parameters

Having described the common polarimetry characteristics of individual elements and their corresponding Mueller matrices for forward modeling, we now turn to the complicated *inverse* problem of separating out the constituent contributions from simultaneous polarization effects.

That is, given a particular Mueller matrix obtained from an unknown complex system, can it be analyzed to extract constituent polarization contributions? Here, we shall discuss an extended Mueller matrix decomposition methodology that enables the extraction of the individual intrinsic polarimetry characteristics from the "lumped" system Mueller matrix [17–19]. In addition to the inverse Mueller matrix decomposition method, we have also developed a polarization sensitive forward Monte Carlo (MC) model capable of simulating all the simultaneous optical (scattering and polarization) effects [20]. This is further supplemented by a high-sensitivity polarization modulation/synchronous detection experimental system capable of measuring the complete Mueller matrix from tissues and tissue-like turbid media [10]. These three methodologies form our comprehensive turbid polarimetry platform. A schematic of this turbid polarimetry platform is shown in Figure 9.1. The (i) experimental polarimetry system and (ii) polarization-sensitive Monte Carlo model are discussed subsequently in Sections 9.4 and 9.5 respectively.

For now, we turn our attention to the inverse Mueller matrix decomposition method [part (iii) of Figure 9.1]. The method consists of decomposing a given Mueller matrix $\mathbf{M}$ into the product of three "basis" matrices [19]

$$\mathbf{M} = \mathbf{M}_\Delta \mathbf{M}_R \mathbf{M}_D, \tag{9.13}$$

representing a depolarizer matrix $\mathbf{M}_\Delta$ to account for the depolarizing effects of the medium, a retarder matrix $\mathbf{M}_R$ to describe the effects of linear birefringence and optical activity, and a diattenua-

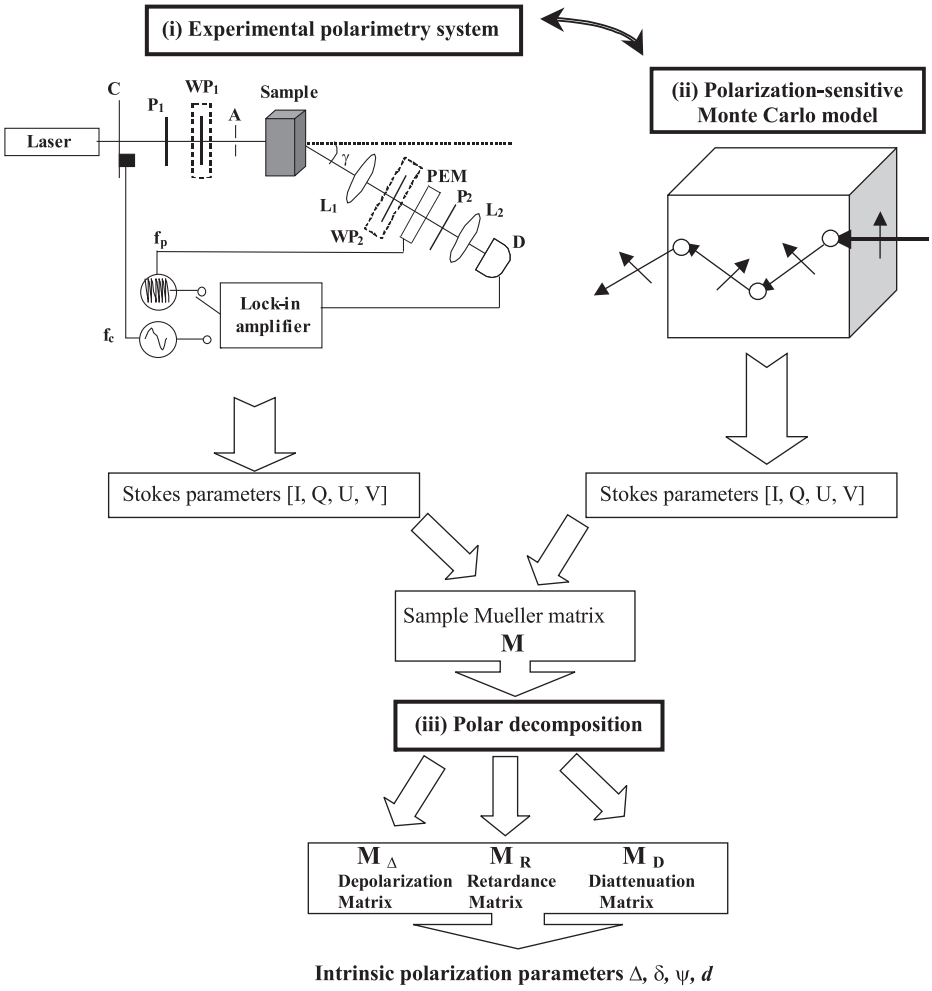

FIGURE 9.1: Schematic of the turbid polarimetry platform: (i) experimental system based on polarization modulation and phase-sensitive synchronous detection, (ii) polarization-sensitive Monte Carlo simulations for forward modeling of simultaneous polarization effects in the presence of turbidity, and (iii) the polar decomposition of the Mueller matrix to inverse calculate the constituent polarization contributions in complex turbid media. In the experimental system (i): C, mechanical chopper; P_1, P_2, polarizers; WP_1, WP_2, removable quarter wave plates; A, aperture; L_1, L_2 lenses; PEM, photoelastic modulator; D, photodetector; f_c, f_p modulation frequencies of mechanical chopper and PEM, respectively. The detection optics can be rotated by an angle γ around the sample.

tor matrix $\mathbf{M}_D$ to include the effects of linear and circular diattenuation. The validity of this decomposition procedure was first demonstrated in optically *clear* media by Lu and Chipman [19]. Here, we extend their analysis to encompass complex tissue-like turbid media. Once calculated, these constituent matrices can further be analyzed to derive quantitative individual polarization medium properties, as summarized below [17, 19, 21]. The diattenuation matrix $\mathbf{M}_D$ is defined as

$$\mathbf{M}_D = \begin{bmatrix} 1 & \bar{d}^T \\ \bar{d} & m_D \end{bmatrix}, \tag{9.14}$$

where m_D is a 3×3 submatrix, the standard form of which is

$$m_D = \sqrt{(1-d^2)}I + (1-\sqrt{(1-d^2)})\,\hat{d}\,\hat{d}^T, \tag{9.15}$$

where I is the 3×3 identity matrix, $\vec{d}$ is diattenuation vector and $\hat{d}$ is its unit vector, defined as

$$\vec{d} = \frac{1}{M(1,1)}[M(1,2)M(1,3)M(1,4)]^T \qquad \text{and} \qquad \hat{d} = \frac{\vec{d}}{|\vec{d}|}. \tag{9.16}$$

The magnitude of diattenuation $|\vec{d}|$ can be determined as

$$d = \frac{1}{M(1,1)}\sqrt{M(1,2)^2 + M(1,3)^2 + M(1,4)^2}. \tag{9.17}$$

Here $M(i,j)$ are elements of the original sample Mueller matrix $\mathbf{M}$. The coefficients $M(1,2)$ and $M(1,3)$ represent linear diattenuation for horizontal (vertical) and $+45^\circ(-45^\circ)$ linear polarization respectively and the coefficient $M(1,4)$ represents circular diattenuation; this can be seen from the original definition of the Stokes/Mueller formalism [Eq. (9.7)].

Having dealt with diattenuation, the product of the retardance and the depolarizing matrices follows from Eq. (9.13) as

$$\mathbf{M}_\Delta \mathbf{M}_R = \mathbf{M}' = \mathbf{M}\,\mathbf{M}_D^{-1}. \tag{9.18}$$

The matrices $\mathbf{M}_\Delta$, $\mathbf{M}_R$ and $\mathbf{M}'$ have the following form

$$\mathbf{M}_\Delta = \begin{bmatrix} 1 & \vec{0}^T \\ P_\Delta & m_\Delta \end{bmatrix}; \quad \mathbf{M}_R = \begin{bmatrix} 1 & \vec{0}^T \\ \vec{0} & m_R \end{bmatrix}; \quad \text{and} \quad \mathbf{M}' = \begin{bmatrix} 1 & \vec{0}^T \\ P_\Delta & m' \end{bmatrix} \tag{9.19}$$

Here $P_\Delta = (\vec{P} - m\vec{d})/(1-d^2)$, the Polarizance vector $\vec{P} = M(1,1)^{-1}[M(2,1)M(3,1)M(4,1)]^T$ [m_Δ and m_R are 3×3 submatrices of $\mathbf{M}_\Delta$ and $\mathbf{M}_R$]. Similarly, m' is a 3×3 submatrix of $\mathbf{M}'$ and can be written as

$$m' = m_\Delta m_R. \tag{9.20}$$

The submatrix m_Δ can be computed by solving the eigenvalue problem for the matrix $m'\,m'^T$ [19]. This can then be used to construct the depolarization matrix $\mathbf{M}_\Delta$. From the elements of $\mathbf{M}_\Delta$, net depolarization coefficient Δ can be calculated as

$$\Delta = \frac{1}{3}|\mathrm{Tr}(\mathbf{M}_\Delta) - 1|. \tag{9.21}$$

Finally, the expression for the retardance submatrix can be obtained from Eq. (9.20) as

$$m_R = m_\Delta^{-1}\,m'. \tag{9.22}$$

From Eq. (9.19) and (9.22), the total retardance $\mathbf{M}_R$ matrix can be computed.

The value for total retardance (R is a parameter that represents the combined effect of linear and circular birefringence) can be determined from the decomposed retardance matrix $\mathbf{M}_R$ using the relationship

$$R = \cos^{-1}\left\{\frac{\mathrm{Tr}(\mathbf{M}_R)}{2} - 1\right\}. \tag{9.23}$$

$\mathbf{M}_R$ can be further expressed as a combination of a matrix for a linear retarder (having a magnitude of linear retardance δ, its retardance axis at angle θ with respect to the horizontal) and a circular

retarder (optical rotation with magnitude of ψ). Using the standard forms of the linear retardance and optical rotation matrices [Eq. (9.10) and (9.11)], the relationship between total retardance (R), optical rotation (ψ) and linear retardance (δ) can be worked out as [19]

$$R = \cos^{-1}\left\{2\cos^2(\psi)\cos^2(\delta/2) - 1\right\}. \tag{9.24}$$

The values for optical rotation (ψ) and linear retardance (δ) can be determined from the elements of the matrix $\mathbf{M}_R$ as [17, 21]

$$\delta = \cos^{-1}\left(\sqrt{\left(\mathbf{M_R}(2,2) + \mathbf{M_R}(3,3)\right)^2 + \left(\mathbf{M_R}(3,2) - \mathbf{M_R}(2,3)\right)^2} - 1\right) \tag{9.25}$$

and

$$\psi = \tan^{-1}\left(\frac{\mathbf{M_R}(3,2) - \mathbf{M_R}(2,3)}{\mathbf{M_R}(2,2) + \mathbf{M_R}(3,3)}\right). \tag{9.26}$$

An interesting problem is that the multiplication order in Eq. (9.13) is ambiguous (due to the noncommuting nature of matrix multiplication, $\mathbf{M}_A\mathbf{M}_B \neq \mathbf{M}_B\mathbf{M}_A$), so that six different decompositions (order of multiplication) are possible. It has been shown that the six different decompositions can be grouped in two families, depending upon the location of the depolarizer and the diattenuator matrices [19, 22, 23]. The three decompositions with the depolarizer set after the diattenuator form the first family (of which Eq. (9.13) is a particular sequence). On the other hand, the three decompositions with the depolarizer set before the diattenuator constitute the other family.

$$\begin{array}{lll} & \mathbf{M} = \mathbf{M}_{\Delta}\mathbf{M}_{R}\mathbf{M}_{D} & \qquad\qquad \mathbf{M} = \mathbf{M}_{D}\,\mathbf{M}_{R}\mathbf{M}_{\Delta} \\ (M_{\Delta D} \quad \text{family}) & \mathbf{M} = \mathbf{M}_{\Delta}\mathbf{M}_{D}\,\mathbf{M}_{R} & (M_{D\Delta} \quad \text{family}) \quad \mathbf{M} = \mathbf{M}_{R}\mathbf{M}_{D}\,\mathbf{M}_{\Delta}. \\ & \mathbf{M} = \mathbf{M}_{R}\mathbf{M}_{\Delta}\mathbf{M}_{D} & \qquad\qquad \mathbf{M} = \mathbf{M}_{D}\,\mathbf{M}_{\Delta}\mathbf{M}_{R} \end{array} \tag{9.27}$$

It has been shown that among the six decompositions, product in Eq. (9.13) or its reverse order ($\mathbf{M} = \mathbf{M}_D\,\mathbf{M}_R\,\mathbf{M}_\Delta$) always produce a physically realizable Mueller matrix [23]. The other possible decompositions can be obtained using similarity transformations, for each of the two individual families. It is thus favorable to use these two orders of decomposition when nothing is known *a priori* about an experimental Mueller matrix.

To summarize, we have presented a mathematical methodology of matrix decomposition to separate out the individual intrinsic polarimetry characteristics from "lumped" Mueller matrix obtained from an unknown complex system. Its validation and initial biological applications are described later. In the following section, we describe a high-sensitivity polarization modulation/synchronous detection experimental system for the measurement of Mueller matrix in tissue-like turbid media.

9.4 Sensitive Experimental System for Mueller Matrix Measurements in Turbid Media

In order to measure polarization signals in strongly depolarizing scattering media such as biological tissues, a highly sensitive polarimetry system is required. Multiple scattering leads to depolarization of light, creating a large depolarized source of noise that hinders the detection of the small residual polarization-retaining signal. One possible method to detect these small polarization signals is the use of polarization modulation with synchronous lock-in-amplifier detection. Many types of detection schemes have been proposed with this approach [10, 11, 13]. Some of these perform polarization modulation on the light that is incident on the sample; others modulate the

sample-emerging light, by placing the polarization modulator between the sample and the detector. The resultant signal can be analyzed to yield sample-specific polarization properties that can then be linked to the quantities of interest. We describe here a specific experimental embodiment of the polarization modulation/synchronous detection approach. This arrangement carries the advantage of being assumption-independent, in that no functional form of the sample polarization effects is assumed [10]. This is important for polarimetric characterization of complex media such as tissues, since there are typically several polarization-altering effects occurring simultaneously. In such situations, it is preferable to have an approach that does not require assumptions on how tissue alters polarized light, but rather determines it directly.

A schematic of the experimental turbid polarimetry system was shown in Figure 9.1 [part (i)] [10]. Unpolarized light at 632.8 nm from a He-Ne laser is used to seed the system. The light first passes through a mechanical chopper operating at a frequency $f_c \sim 500$ Hz; this is used in conjunction with lock-in amplifier detection to accurately establish the overall signal intensity levels. Recording of the full (4×4) Mueller matrix requires generation of the four input polarization states, 0° (Stokes vector $[1\ 1\ 0\ 0]^T$), 45° (Stokes vector $[1\ 0\ 1\ 0]^T$), and 90° (Stokes vector $[1\ -1\ 0\ 0]^T$) linear polarizations, as well as circular polarization (Stokes vector $[1\ 0\ 0\ 1]^T$), which is enabled by the input optics (a linear polarizer P_1 with/without the quarter wave plate WP_1). The sample-scattered light is detected at a chosen angle (γ) as the detection optics can be rotated around the sample. The detection optics begin with a removable quarter wave plate (WP_2) with its fast axis oriented at -45°, when in place allowing for the measurement of Stokes parameters Q and U (linear polarization descriptors), and when removed allowing for the measurement of Stokes parameter V (circular polarization descriptor). The light then passes through a photoelastic modulator (PEM), which is a linearly birefringent resonant device operating at $f_p = 50$ kHz. The fast axis of the PEM is at 0° and its retardation is modulated according to the sinusoidal function $\delta_{\mathrm{PEM}}(t) = \delta_o \sin\omega t$, where $\omega_p = 2\pi f_p$ and δ_o is the user-specified amplitude of maximum retardation of PEM. The light finally passes through a linear analyzer orientated at 45°, converting the PEM-imparted polarization modulation to an intensity modulation suitable for photodetection. The resulting modulated intensity is collected using a pair of lenses (detection area of 1 mm^2 and acceptance angle $\sim 18^\circ$) and is relayed to an avalanche photodiode detector. The detected signal is sent to a lock-in amplifier, with its reference input toggling between the frequencies of the chopper (500 Hz) and the PEM controller (50 kHz and harmonics) for synchronous detection of their respective signals.

For a given polarization state of the incident light, the Stokes vector of light after the analyzing block $[I_f Q_f U_f V_f]^T$, can be related to that of the sample-emerging beam $[IQUV]^T$ as (with detection quarter wave-plate in place) [10]

$$\begin{pmatrix} I_f \\ Q_f \\ U_f \\ V_f \end{pmatrix} = \frac{1}{2} \underset{P_2}{\begin{pmatrix} 1 & 0 & 1 & 0 \\ 0 & 0 & 0 & 0 \\ 1 & 0 & 1 & 0 \\ 0 & 0 & 0 & 0 \end{pmatrix}} \underset{\mathrm{PEM}}{\begin{pmatrix} 1 & 0 & 0 & 0 \\ 0 & 1 & 0 & 0 \\ 0 & 0 & \cos\delta & \sin\delta \\ 0 & 0 & -\sin\delta & \cos\delta \end{pmatrix}} \underset{WP_2}{\begin{pmatrix} 1 & 0 & 0 & 0 \\ 0 & 0 & 0 & 1 \\ 0 & 0 & 1 & 0 \\ 0 & -1 & 0 & 0 \end{pmatrix}} \begin{pmatrix} I \\ Q \\ U \\ V \end{pmatrix}, \tag{9.28}$$

and when the detection quarter wave-plate is removed as

$$\begin{pmatrix} I_{fr} \\ Q_{fr} \\ U_{fr} \\ V_{fr} \end{pmatrix} = \frac{1}{2} \underset{P_2}{\begin{pmatrix} 1 & 0 & 1 & 0 \\ 0 & 0 & 0 & 0 \\ 1 & 0 & 1 & 0 \\ 0 & 0 & 0 & 0 \end{pmatrix}} \underset{\mathrm{PEM}}{\begin{pmatrix} 1 & 0 & 0 & 0 \\ 0 & 1 & 0 & 0 \\ 0 & 0 & \cos\delta & \sin\delta \\ 0 & 0 & -\sin\delta & \cos\delta \end{pmatrix}} \begin{pmatrix} I \\ Q \\ U \\ V \end{pmatrix}. \tag{9.29}$$

The detected time-dependent intensities are thus

$$I_f(t) = \frac{I}{2}\left[1 - q\sin\delta + u\cos\delta\right], \tag{9.30}$$

and

$$I_{fr}(t) = \frac{I}{2}\left[1 - v\sin\delta + u\cos\delta\right], \tag{9.31}$$

Here $q = Q/I$, $u = U/I$, and $v = V/I$, and δ is the time-dependent PEM retardation, $\delta = \delta_0 \sin\omega t$. The time-varying circular function in the argument of another circular function of Eq. (9.30) and (9.31) can be expanded in Fourier series of Bessel functions, to yield signals at different harmonics of the fundamental modulation frequency. It can be advantageous in terms of SNR to choose the peak retardance of the PEM such that the zeroth order-Bessel function J_0 is zero [10]; with δ_o = 2.405 radians (resulting in $J_0(\delta_o)$ = 0), Fourier-Bessel expansion of Eq. (9.30) and (9.31) gives

$$I_f(t) = \frac{1}{2}\left[1 - 2J_1(\delta_0)q\sin\omega t + 2J_2(\delta_0)u\cos 2\omega t + \ldots\right], \tag{9.32}$$

and

$$I_{fr}(t) = \frac{1}{2}\left[1 - 2J_1(\delta_0)v\sin\omega t + 2J_2(\delta_0)u\cos 2\omega + \ldots\right]. \tag{9.33}$$

The normalized Stokes parameters of the sample-scattered light (q, u, and v) can thus be obtained from synchronously-detected signals at the chopper frequency V_{1fc} (the dc signal level), and at the first and second harmonics of the PEM frequency V_{1fp} and V_{2fp} respectively. The experimentally measurable waveform in terms of the detected voltage signal is,

$$V(t) = V_{1fc} + \sqrt{2}V_{1fp}\sin\omega t + \sqrt{2}V_{2fp}\cos 2\omega t + \ldots, \tag{9.34}$$

with $\sqrt{2}$ factor taking into account the RMS nature of lock-in detection [10]. Applying Eq. (9.34) to the detected signal with the detection wave plate in the analyzer arm [Eq. (9.32)] gives

$$V_{1fc} = \frac{I}{2}k, \qquad \sqrt{2}V_{1f} = -IkJ_1(\delta_0)q, \qquad \sqrt{2}V_{2f} = IkJ_2(\delta_0)u, \tag{9.35}$$

where k is an instrumental constant, same for all equations. The normalized linear polarization Stokes parameters q and u are then obtained from,

$$q = \frac{V_{1fp}}{\sqrt{2}J_1(\delta_o)V_{1fc}}, \tag{9.36}$$

and

$$u = \frac{V_{2fp}}{\sqrt{2}J_2(\delta_o)V_{1fc}}, \tag{9.37}$$

Comparing Eqs. (9.34) and (9.33) when the detection quarter wave plate is removed yields

$$V_{1fc} = \frac{I}{2}k \tag{9.38}$$

$$\sqrt{2}V_{1f} = -IkJ_1(\delta_0)v,$$

and the circular polarization Stokes parameter v is then obtained as,

$$v = \frac{V_{1fp}}{\sqrt{2}J_1(\delta_0)V_{1fc}}. \tag{9.39}$$

The preceding discussion of experimental determination of Stokes vector descriptors deals with quantifying the polarization state of the sample-scattered light; we now turn our attention explicitly to determining the polarization properties of the sample as described by its Mueller matrix. In order to perform measurements of the full (4×4) Mueller matrix, the input polarization is cycled between four states (linear polarization at 0°, 45°, 90°, and right circular polarization) and the output Stokes vector for each respective input state is measured. The elements of the resulting 4 measured Stokes vectors can be analyzed to yield the sample Mueller matrix as [17]

$$\mathbf{M}(i,j)=\begin{bmatrix} \frac{1}{2}(I_H+I_V) & \frac{1}{2}(I_H-I_V) & I_p-\mathbf{M}(1,1) & I_R-\mathbf{M}(1,1) \\ \frac{1}{2}(Q_H+Q_V) & \frac{1}{2}(Q_H-Q_V) & Q_p-\mathbf{M}(2,1) & Q_R-\mathbf{M}(2,1) \\ \frac{1}{2}(U_H+U_V) & \frac{1}{2}(U_H-U_V) & U_p-\mathbf{M}(3,1) & U_R-\mathbf{M}(3,1) \\ \frac{1}{2}(V_H+V_V) & \frac{1}{2}(V_H-V_V) & V_p-\mathbf{M}(4,1) & V_R-\mathbf{M}(4,1) \end{bmatrix}. \tag{9.40}$$

Here, the four input states are denoted with the subscripts H (0°), P (45°), V (90°), and R (right circularly polarized; left circular incidence can be used as well, resulting only in a sign change). The indices $i,j=1,2,3,4$ denote rows and columns respectively.

The described experimental approach based on polarization modulation and synchronous detection is suitable for sensitive polarimetric detection in turbid media. This experimental system has been used to carry out several fundamental studies on turbid medium polarimetry and for polarization-based characterization of biological tissues. Some of these studies are described in Section 9.6, and 9.8 of this chapter. For now, we turn to the equally challenging problems of accurately forward modeling the polarization signals in turbid media (part (ii) of Figure 9.1, Section 9.5).

9.5 Forward Modeling of Simultaneous Occurrence of Several Polarization Effects in Turbid Media Using the Monte Carlo Approach

To aid in the investigation of polarized light propagation in turbid media such as biological tissue, accurate modeling is enormously useful for gaining physical insight, designing and optimizing experiments, and analyzing measured data. The Maxwell's equations-based electromagnetic theoretical approach is the most rigorous and best-suited method for polarimetric analysis; however, solving Maxwell's equations for polarized light propagation in multiple scattering media is impractical. Alternatively, light propagation through scattering media can in principle be modeled through transport theory; however, transport theory and its simplified variant, the diffusion approximation, are both intensity-based techniques, and hence typically neglect polarization [24]. A more general and robust approach is the Monte Carlo technique [24]. In this statistical approach to radiative transfer, the multiple scattering trajectories of individual photons are determined using a random number generator to predict the probability of each scattering event. The superposition of many photon paths approaches the actual photon distribution in time and space. This approach has the advantage of being applicable to arbitrary geometries and arbitrary optical properties. The first Monte Carlo models were also developed for intensity calculations only and neglected polarization information [25]. More recently, a number of implementations have incorporated polarization into their Monte Carlo models [26]. Currently, the Monte Carlo technique is the most general approach to simulate polarized light propagation in scattering media, although long computation times are often required to generate statistically meaningful results.

A flowchart for polarization-sensitive Monte Carlo model is shown in Figure 9.2. In this modeling, it is assumed that scattering events occur independently and exhibit no coherence effects. The position, propagation direction, and polarization of each photon are initialized and modified as the

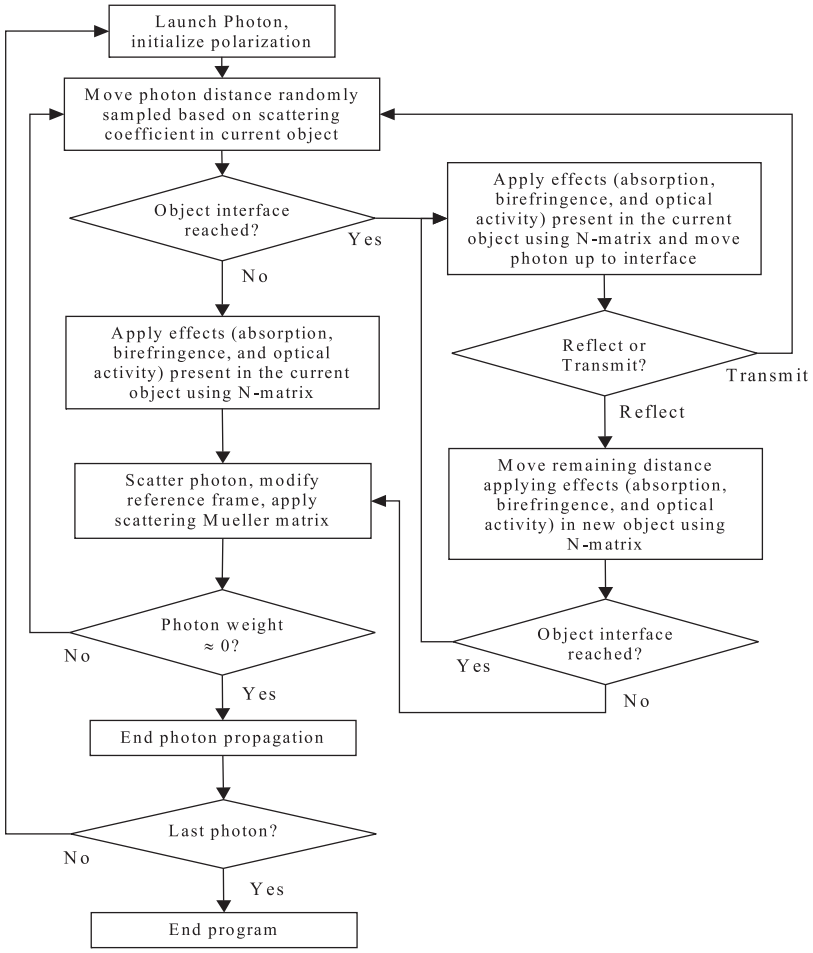

FIGURE 9.2: Flowchart for polarization-sensitive Monte Carlo model. The polarization effects are applied using medium Mueller matrices. The Mueller matrix for scattering is calculated using Mie theory and that for other simultaneously occurring effects (birefringence and optical activity) are calculated using N-matrix approach (see text).

photon propagates through the scattering medium. The photon's polarization, with respect to a set of arbitrary orthonormal axes defining its reference frame, is represented as a Stokes vector **S** and polarization effects are applied using medium Mueller matrices **M** [11, 27]. The photon propagates in the sample between scattering events a distance l sampled from the probability distribution $\exp(-\mu_t l)$. Here, the extinction coefficient μ_t is the sum of the absorption μ_a and scattering μ_s coefficients and l is the distance traveled by the photon between scattering events. When the photon encounters a scattering event, a scattering plane and angle are statistically sampled based on the polarization state of the photon and the Mueller matrix of the scatterer.

The photon's reference frame is first expressed in the scattering plane and then transformed to the laboratory (experimentally observable) frame through multiplication by a Mueller matrix calculated through Mie scattering theory [28]. Upon encountering an interface (either an internal one, representing tissue domains of different optical properties, or an external one, representing exter-

nal tissue boundary), the probability of either reflection or transmission is calculated using Fresnel coefficients. As no coherence effects are considered, the final Stokes vector for light exiting the sample in a particular direction is computed as the sum of all the appropriate directional photon subpopulations. Various quantities of interest such as detected intensities, polarization properties (Stokes vectors, Mueller matrices), average pathlengths, and so forth, can be quantified once a sufficient number of photon (packets) have been followed and tracked to generate statistically acceptable results (typically 10^7–10^9 photons).

However, most current Monte Carlo models of polarized light propagation do not fully simulate all of the polarization effects of tissue. This is primarily due to the inherent difficulty in formulating *simultaneous* polarization effects, especially in the presence of multiple scattering. As discussed previously, multiplication of the Mueller matrices for individual polarization effects is not commutative, thus, different orders in which these effects are applied will have different effects on the polarization. Ordered multiplication of these matrices does not make physical sense, as in biological tissue these effects (such as optical activity due to chiral molecules and linear birefringence due to anisotropic tissue structures) are exhibited simultaneously, and not one after the other as sequential multiplication implies. Fortunately, a method exists to simulate simultaneous polarization effect in *clear* media through the so-called *N*-matrix formalism, which combines the effects into a single matrix describing them simultaneously [29]. The *N*-matrix formalism was thus employed in the polarization-sensitive Monte Carlo simulation code in tissue-like media to model *simultaneous* polarization effects *between* scattering events in the presence of multiple scattering.

The *N*-matrix approach was first developed by Jones [29], and a more thorough derivation is provided in Kliger et al. [3]. Briefly, in this approach the sample matrix is represented as an exponential function of a *sum* of matrices, where each matrix in the sum corresponds to a single optical polarization effect. The issue of ordering of noncommutative multiplying matrices disappears as matrix addition is always commutative, and applies to differential matrices representing the optical property over an infinitely small optical pathlength. These differential matrices, known as *N*-matrices, correspond to each optical property exhibited by the sample and are summed to express combined effect. The formalism is expressed in terms of 2×2 Jones matrices applicable to clear nondepolarizing media, rather than the more commonly used 4×4 Mueller matrices. However, a Jones matrix can be converted to a Mueller matrix provided there are no depolarization effects [15]. This is indeed applicable to our Monte Carlo model, as depolarization is caused by the multiple scattering events, and no depolarization effects occur *between* the scattering events. Once converted to the Mueller matrix formalism, this modified *N*-matrix approach was then applied to the photons as they propagate between scattering events in the MC simulation. This approach enabled the combination of any number of simultaneously occurring polarizing effects [in our case, circular birefringence (optical activity) and linear birefringence were incorporated, since these are the most prominent tissue polarimetry effects] [20].

In the simulations, circular and linear birefringence were modeled through the optical activity χ in degrees per centimeter, and through the anisotropy in refractive indices (Δn), respectively. Here, $\Delta n = (n_e - n_o)$ is the difference in the refractive index along the extraordinary axis (n_e) and the ordinary axis (n_o). For simplicity, it was assumed that the medium is uni-axial and that the direction of the extraordinary axis and the value for Δn is constant throughout the scattering medium. In each simulation, n_e and n_o were taken as input parameters and a specific direction of the extraordinary axis was chosen. As each photon propagates between scattering events, the difference in refractive indices seen by the photon depends on the propagation direction with respect to the extraordinary axis. The effect was modeled using standard formulae describing the angular variation of the refractive index in a uni-axial medium [20].

The ability of the extended polarization-sensitive Monte Carlo model to simulate *simultaneous* polarization effects in the presence of multiple scattering was experimentally validated in solid polyacrylamide phantoms exhibiting simultaneous linear birefringence, optical activity, and depolarization [20]. These were developed using polyacrylamide as a base medium, with sucrose-induced

optical activity, polystyrene microspheres-induced scattering (mean diameter $D = 1.40\mu$m, refractive index $n_s = 1.59$), and mechanical stretching to cause linear birefringence (or linear retardance). To apply controllable strain to produce linear birefringence, one end of the polyacrylamide phantoms (dimension of $1 \times 1 \times 4$ cm) was clamped to a mount and the other end to a linear translational stage. The phantoms were stretched along the vertical direction (the long axis of the sample) to introduce varying linear birefringence with its axis along the direction of strain. Measurements of the Stokes parameters (normalized Stokes parameters $q = Q/I,\ u = U/I,\ v = V/I$) of scattered light (in different geometries) from the phantoms were made using the PEM-based polarimeter (described in the previous section), and compared to the results of Monte Carlo simulations run with similar parameters. Measurements were made from phantoms exhibiting turbidity and birefringence (no added sucrose, i.e, no optical activity), as well as for phantoms exhibiting turbidity, birefringence, and optical activity [20]. In both cases, the Monte Carlo-simulated Stokes parameters were in excellent agreement with the controlled experimental results (for details the reader is referred to Ref. 18). These results provided strong evidence for the validity of the Monte Carlo model. The model can therefore accurately simulate complex tissue polarimetry effects, including simultaneous optical activity and birefringence in the presence of scattering. This, in combination with the experimental turbid polarimetry system (and phantoms), was therefore used to test the efficacy of the Mueller matrix decomposition approach to delineate individual intrinsic polarimetry characteristics in complex tissue-like turbid media. Some of these studies are now described.

9.6 Validation of the Mueller Matrix Decomposition Method in Complex Tissue-Like Turbid Media

Previously employed for examination of nonscattering media, the extended Mueller matrix decomposition methodology (described in Section 9.3) has seen only initial use in turbid media, and as such requires validation. The validity of the matrix decomposition approach summarized in Eqs. (9.13)–(9.27) in complex turbid media was therefore tested with both experimental (Section 9.4) and MC-simulated (Section 9.5) Mueller matrices, whose constituent properties are known and user-controlled *a priori* [17,18].

In the experimental studies, the PEM-based polarimeter (Figure 9.1) was used to record Mueller matrices in the forward detection geometry (sample thickness = 1 cm, detection area of 1 mm^2, and an acceptance angle $\sim 18^\circ$ around $\gamma = 0^\circ$ direction were used) from a solid polyacrylamide phantom (discussed in the previous section) that mimics the complexity of biological tissues, in that it exhibits simultaneous linear birefringence, optical activity, and depolarization [10, 17, 20].

Figure 9.3 and Table 9.1 show the experimental Mueller matrix and the corresponding decomposed depolarization ($\mathbf{M}_\Delta$), retardance ($\mathbf{M}_R$), and diattenuation ($\mathbf{M}_D$) matrices from a birefringent (extension = 4 mm), chiral (magnitude of optical activity was χ = 1.96degree cm^{-1}, corresponding to 1 M concentration of sucrose), turbid phantom (scattering coefficient of μ_s = 30 cm^{-1} and anisotropy parameter g = 0.95). The complicated nature of the resultant Mueller matrix $\mathbf{M}$, with essentially all 16 nonzero matrix elements, underscores the problem at hand – how does one extract useful sample metrics from this wealth of intertwined information? In contrast, the three basis matrices derived from the decomposition process exhibit simpler structures with many zero off-diagonal elements, and are directly amenable for further quantification. Equations (9.17), (9.21), (9.25), and (9.26) were applied to the decomposed basis matrices to retrieve the individual polarization parameters (d, Δ, δ, and ψ). The determined values for these are also listed in Table 9.1.

The comparison of the derived and the input control values for the polarization parameters reveals several interesting trends. The expected value for diattenuation d is zero, whereas the decomposition

TABLE 9.1: The values for the polarization parameters extracted from the decomposed matrices (2nd column). The input control values for linear retardance δ and optical rotation ψ (3rd column) were obtained from measurement on a clear ($\mu_s = 0\ \text{cm}^{-1}$) phantom having the same extension (= 4 mm) and similar concentration of sucrose (1 M) as that of the turbid phantom, and corrected for the increased pathlength due to multiple scattering (determined from Monte Carlo modeling). The expected value for the net depolarization coefficient Δ was determined from the Monte Carlo simulation of the experiment. (Adopted from [17]).

Parameters	Estimated value (from $\mathbf{M}_\Delta$, $\mathbf{M}_R$, $\mathbf{M}_D$)	Expected value
d	0.03	0
δ	1.38 rad	1.34 rad
ψ	2.04°	2.07°
Δ	0.21	0.19

method yields a small but nonzero value of d = 0.03. Scattering-induced diattenuation that arises primarily from singly (or weakly) scattered photons [20] is not expected to contribute here, because multiply scattered photons are the dominant contributors to the detected signal in the forward detection geometry. Hence, the presence of small amount of dichroic absorption (at the wavelength of excitation λ = 632.8 nm) due to anisotropic alignment of the polymer molecules in the polyacrylamide phantom possibly contribute to this slight nonzero value for the parameter d.

The derived decomposition value of $\Delta = 0.21$ seems reasonable, although this is difficult to compare with theory (there is no direct link between the scattering coefficient and resultant depolarization). The value shown in the theoretical comparison column of the Table was determined from the Monte Carlo simulation of the experiment, as described in the previous section. The resultant agreement in the depolarization values is excellent. It is worth noting that decomposition results for an analogous purely depolarizing phantom (same turbidity, no birefringence nor chirality – results not

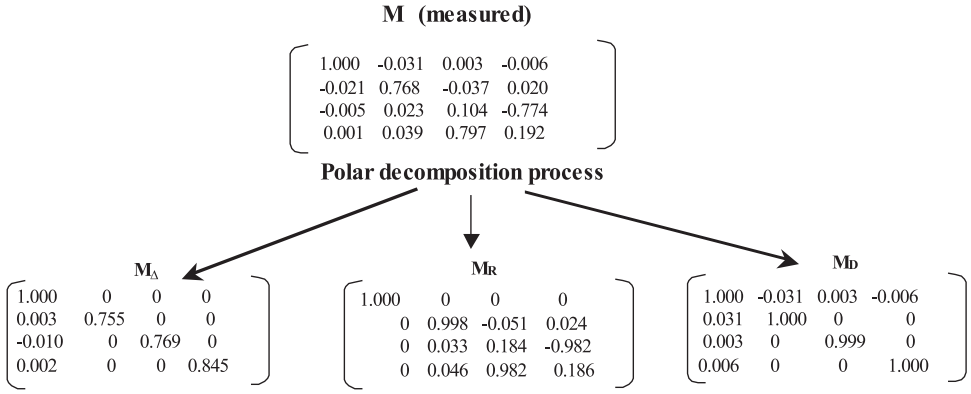

FIGURE 9.3: The experimentally recorded Mueller matrix and the decomposed matrices for a birefringent (extension = 4 mm), chiral (concentration of sucrose = 1 M, $\chi = 1.96°$ / cm), turbid (μ_s = 30 cm^{-1}, g = 0.95, thickness t = 1 cm) phantom (Adopted from [17]).

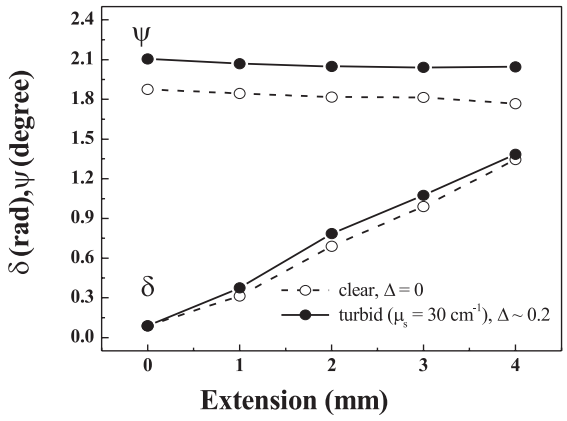

FIGURE 9.4: Linear retardance δ and optical rotation ψ estimated from the decomposition of *experimentally* recorded Mueller matrices from solid chiral (χ = 1.96° cm^{-1}, corresponding to 1 M concentration of sucrose) phantoms having varying degrees of strain-induced birefringence (extension of 0–4 mm, $\delta = 0$–1.345). Results are shown for both clear ($\mu_s = 0$ cm^{-1}) and turbid ($\mu_s = 30$ cm^{-1}, $g = 0.95$) phantoms. The measurements were performed in the forward direction (γ = 0°) through a 1 cm × 1 cm × 4 cm phantom. The points represent decomposition-derived values and the lines are guide for the eye for this and all subsequent figures. (Adopted from [17]).

shown) were within 5% of the above Δ values [17]. This self-consistency implied that decomposition process successfully decouples the depolarization effects due to multiple scattering from linear retardation and optical rotation contributions, thus yielding accurate and quantifiable estimates of the δ and ψ parameters in the presence of turbidity.

The Mueller-matrix derived value of optical rotation $\psi = 2.04°$ of the turbid phantom was, however, slightly larger than the corresponding value measured from a clear phantom having the same concentration of sucrose ($\psi_0 = 1.77°$). This small increase in the ψ value in the presence of turbidity is likely due to an increase in optical path length engendered by multiple scattering. Indeed, the value for ψ, calculated using the optical rotation value for the clear phantom (ψ_0 = 1.77°) and the value for average photon path length ($\langle L \rangle = 1.17$ cm, determined from Monte Carlo simulations [20]) [$\psi = \psi_0 \times \langle L \rangle = 2.07°$] was reasonably close to the decomposition-derived value from the experimental Mueller matrix (ψ = 2.04°).

Although the estimated value for retardance δ of the turbid phantom is slightly larger than that for the clear phantom ($\delta = 1.38$ rad for the turbid phantom, as compared to 1.34 rad for the clear phantom), the value is significantly lower than that one would expect for average photon path length of 1.17 cm ($\delta = 1.34 \times 1.17 = 1.57$ rad). This can be seen from Figure 9.4, where the estimates for δ and ψ of the chiral (χ = 1.96° cm^{-1}) phantoms having varying degree of strain induced birefringence (extension of 0–4 mm) are displayed [17]. The increase in the value for ψ as a result of increased average photon path length in the turbid phantom as compared to the clear phantom is clearly seen. The gradual decrease in the value for ψ with increasing longitudinal stretching is consistent with resulting lateral contraction of the phantom, reducing the effective path length. In contrast to ψ, the expected increase in δ as a result of increased average photon path length in the turbid phantom (compared to clear medium) is not that apparent.

Figure 9.5 shows the derived linear retardance δ and optical rotation ψ parameters, using Monte Carlo-generated Mueller matrices, with chiral molecule concentration as the independent variable [30]. Again, both the clear and turbid values compare well to the input parameter values ($\delta \approx 1.4$ rad

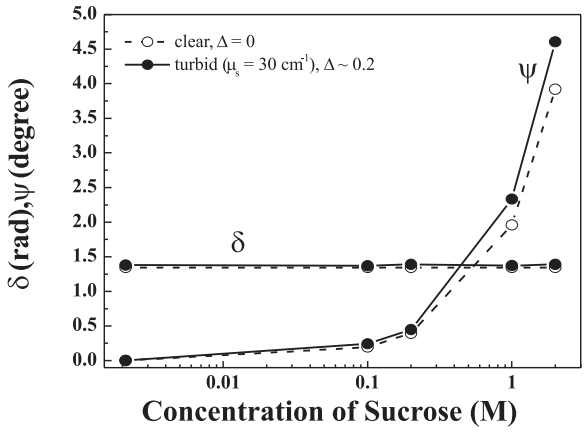

FIGURE 9.5: δ and ψ estimated from the decomposition of *Monte Carlo*-generated Mueller matrices from birefringent media (linear birefringence $\Delta n = 1.36 \times 10^{-5}$, corresponding to $\delta = 1.345$ rad [4 mm extension of 4 cm long phantom] for a path length of 1 cm, the axis of linear birefringence was kept along the vertical direction, orientation angle $\theta = 90^{\circ}$) having varying levels of chirality ($\chi = 0, 0.196, 0.392, 1.96$ and 3.92° cm^{-1}, corresponding to concentration of sucrose of 0, 0.1, 0.2, 1 and 2 M, respectively). Results are shown for both clear ($\mu_s = 0$ cm^{-1}) and turbid ($\mu_s = 30$ cm^{-1}, $g = 0.95$) media. (Adopted from [30]).

and $\psi \approx 1.96^{\circ}$ at 1 M sucrose), showing self-consistency in inverse decomposition analysis and successful decoupling. Further, in agreement with the experimental results, while the value for ψ of the turbid media is larger than that for the clear media as a result of the increase in optical path length due to multiple scattering, a similar increase in δ value is not observed.

Note that none of these trends could be gleaned from the lumped Mueller matrix, where at best one would have to resort to semi-empirical comparison of changes in selected matrix elements, which contain contributions from several effects. Derivation and quantification of the absolute linear retardance δ and optical rotation ψ values is enabled exclusively by the polar decomposition analysis. Based on these and other continuing validation studies, this approach appears valid in complex tissue-like turbid media.

9.7 Selected Trends: Path length and Detection Geometry Effects on the Decomposition-Derived Polarization Parameters

An interesting finding of the results presented in the previous section was that while the value for the derived optical rotation ψ of the turbid media was consistently larger than that of the clear media as a result of increased average photon path length, a similar increase in linear retardance δ was not observed. Monte Carlo simulations were carried out further to understand this trend, and to investigate the effect of multiple scattering, propagation path, and detection geometry on the decomposition-derived δ and ψ parameters [17]. Here, we shall discuss some selected results of those studies.

The MC results suggested that the lowering of the value of net retardance δ likely arises because the scattered light does not travel in a straight line but rather along many possible curved zig-zag

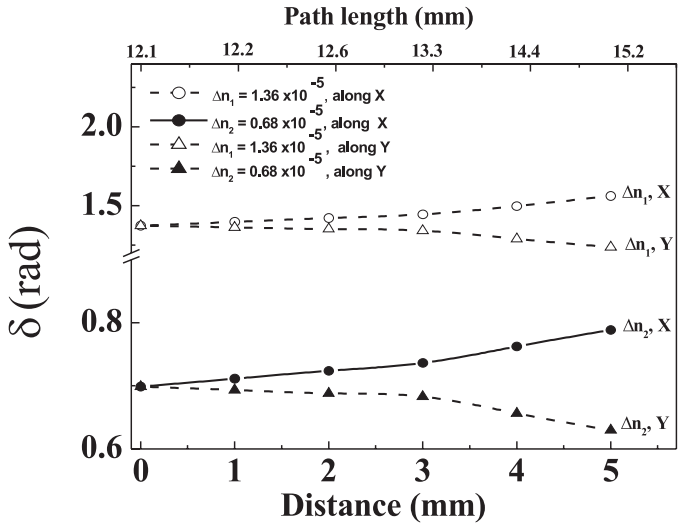

FIGURE 9.6: Variation of δ of transmitted light as a function of distance from ballistic beam position at the exit face of a 1 cm thick birefringent, chiral ($\chi = 1.96^\circ$ cm^{-1}), turbid medium ($\mu_s = 30$ cm^{-1}, $g = 0.95$). The results are shown for two different values of birefringence (Δn = 1.36×10^{-5} and 0.68×10^{-5}). The axis of linear birefringence was kept along the vertical (Y-axis) direction and the results are shown for transmitted light collected at different spatial positions along the horizontal (X-axis) and vertical (Y-axis) direction. The Monte Carlo-calculated average photon path length of light exiting the scattering medium is shown on the top axis. (Adopted from [17]).

paths, the curvature being controlled by the values for μ_s and g. While such paths influence ψ by increasing its value through a relationship with the increasing photon path length, the effect of this on the net value for δ is more complex because a component of the curved propagation paths will be along the direction of the linear birefringence axis (along Y in Figs. 9.6, 9.7)

These results are illustrated in Figures 9.6 and 9.7. Figure 9.6 shows the variation of δ values of transmitted light collected at the exit face of a birefringent ($\Delta n = 1.36 \times 10^{-5}$ and 0.68×10^{-5}), chiral (χ = 1.96° cm^{-1}), turbid medium (μ_s = 30 cm^{-1}, $g = 0.95$, thickness = 1 cm), as a function of distance from the center of the transmitted ballistic beam along the horizontal (X axis, perpendicular to the direction of the axis of birefringence) and vertical (Y axis, parallel to the direction of the axis birefringence) directions. At detector positions along the X axis, δ increases with increasing distance from the center of the ballistic beam (i.e., with increasing average photon path length). In contrast, for detection positions along the Y axis, the value for δ shows gradual decrease with increasing distance from the center of the ballistic beam. This is because a larger component of the photon propagation path is along the axis of birefringence leading to a reduction in net linear retardance δ (because propagation along the direction of the birefringence axis does not yield any retardance [15]). Since such differences in the photon propagation path for the two different detection geometries should have no influence on the value of ψ, the estimates for ψ were found to be identical for similar detection positions either along the X- or the Y-axis at the exit face of the medium (data not shown) [17].

Figure 9.7 demonstrates that for off-axis detection [position coordinate (3,0) or (0,3)], the Mueller matrix-derived δ value vary considerably with a change in the orientation angle (θ) of the birefringence axis. Conversely, for detection around the position of the ballistic beam [coordinate (0, 0)],

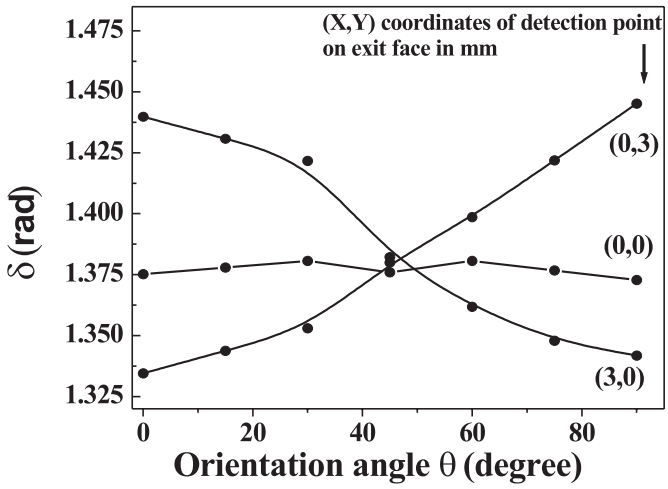

FIGURE 9.7: Variation of δ (estimated from the decomposition of *Monte Carlo-generated* Mueller matrices) as a function of the linear birefringence axis orientation angle θ (with respect to the horizontal) for a birefringent, chiral, turbid medium ($\Delta n = 1.36 \times 10^{-5}$, $\chi = 1.96^{\circ}$ cm^{-1}, $\mu_s = 30$ cm^{-1}, $g = 0.95$, thickness = 1 cm). Results are shown for three different detection positions at the exit face of the medium, detection around the position of the ballistic beam [position coordinate (0,0)], detection at spatial positions 3 mm away from the ballistic beam position along the horizontal (X) [coordinate (3,0)] and vertical (Y) [position coordinate (0,3)] axis, respectively. (Adopted from [17]).

δ is not influenced significantly by a change in θ. Thus, for simultaneous determination of the intrinsic values for the parameters δ and ψ of a birefringent, chiral, turbid medium in the forward scattering geometry, detection around the direction of propagation of the ballistic beam may be preferable [17].

These and other experimental and MC-simulation results on phantoms having varying optical scattering and polarization properties demonstrated that the Mueller matrix decomposition approach can successfully delineate individual intrinsic polarimetry characteristics in complex tissue-like turbid media in the forward detection geometry. Yet the backward detection geometry may be more convenient for many practical applications (particularly for *in situ* measurements). However, the scattering-induced artifacts are more coupled with the intrinsic polarization parameters in the backward detection geometry, partly because of the increasing contribution of the singly or weakly backscattered photons [10, 14, 21]. For example, backscattering induced changes in the orientation angle of the linear polarization vector can manifest themselves as large apparent optical rotation even in absence of chiral molecules in the medium [10, 14]. Decomposition analysis revealed that this large scattering-induced apparent rotation is due to linear diattenuation (difference in amplitude between the scattered light polarized parallel and perpendicular to the scattering plane) [18, 21]. In addition to diattenuation, backscattered photons yields significant values of linear retardance (differences in phase between the scattered light polarized parallel and perpendicular to the scattering plane) even from isotropic ($\Delta n = 0$) scattering medium [18]. This scattering-induced linear retardance interferes with the actual retardance values of a birefringent turbid medium in a complex interrelated way, thus hindering the determination of the latter in the backward detection geometry.

Our studies have shown that the scattering-induced diattenuation and linear retardance are due

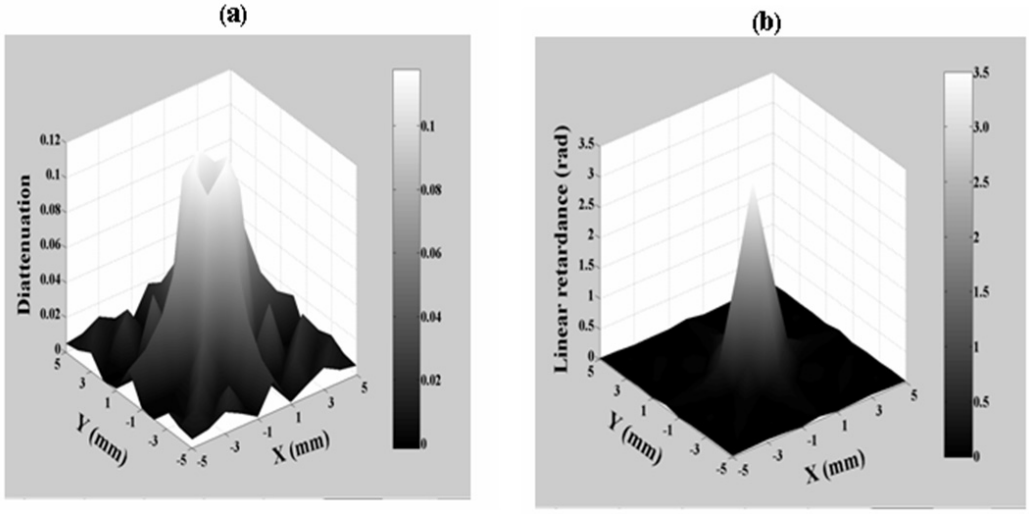

FIGURE 9.8: (a) Diattenuation d and (b) linear retardance δ maps in the backscattering plane ($X-Y$ plane, $Z=0$) derived using decomposition of Monte Carlo-generated Mueller matrices of a nonbirefringent (Δn = 0), achiral ($\chi = 0^\circ$ cm^{-1}), turbid medium (μ_s = 60 cm^{-1}, g = 0.935). The nonzero values for both d and δ results primarily from the confounding effects of singly (weakly) backscattered photons. (Adopted from [18]).

mainly to the singly (or weakly) backscattered photons, and their magnitude is large at detection positions sufficiently close to the exact backscattering direction [18]. As one moves away from the exact backscattering direction, these confounding effects gradually diminish. This is illustrated in Figure 9.8, where the scattering-induced diattenuation (d) and linear retardance (δ) maps in the backscattering plane ($X-Y$ plane, $Z=0$) are shown from a isotropic ($\Delta n = 0$), achiral ($\chi = 0^\circ$ cm^{-1}), turbid medium ($\mu_s = 60$ cm^{-1}, g = 0.935, thickness = 1 cm). These results and further decomposition analyses on Monte Carlo-generated Mueller matrices for turbid media having different scattering coefficients μ_s confirmed that in the backward detection geometry, the effects of scattering-induced linear retardance and diattenuation are weak ($\delta \leq 0.1$ and $d \leq 0.03$) for detection positions located at distances larger than a transport length away from the point of illumination [$r > l_{tr}$, l_{tr} is the transport scattering length $= 1/\mu_s(1-g)$]. Simultaneous determination of the unique intrinsic values of all the polarization parameters from a turbid medium in the backward detection geometry can thus be accomplished by decomposing the Mueller matrix recorded at a distance larger than a transport length away from the point of illumination [18].

Note (as discussed previously in Section 9.3), the multiplication order of the basis matrices in the decomposition analysis [Eq. (9.13)] is ambiguous (due to the noncommuting nature of matrix multiplication). The influence of the order of the matrices in the decomposition analysis on the retrieved polarization parameters was therefore investigated. The experimental and the Monte Carlo-generated Mueller matrices (results presented above) were decomposed following either the order of Eq. (9.13) or its reverse order ($\mathbf{M} = \mathbf{M}_D\,\mathbf{M}_R\,\mathbf{M}_\Delta$). Importantly, the three useful polarization parameters [Δ, ψ, and δ, derived through Eqs. (9.21), (9.25), and (9.26)], were found to be $\sim$independent of the order [difference in their values was in the range 1–5%] [17, 18]. This suggests that the decomposition formalism is self-consistent with respect to the potential ambiguity of ordering. Further work is underway to confirm this initial finding [31].

To summarize Sections 9.6 and 9.7, the applicability of the Mueller matrix decomposition approach in complex tissue-like turbid media (either for the forward or the backward detection ge-

ometry) was validated experimentally with optical phantoms having controlled sample-polarizing properties, and theoretically with a polarization sensitive Monte Carlo model capable of simulating complex tissue polarimetry effects. The individual polarization effects can be successfully decoupled and quantified despite their simultaneous occurrence, even in the presence of the numerous complexities due to multiple scattering. The ability to isolate individual polarization properties provides a valuable noninvasive tool for their quantification and may be relevant for biological tissue examinations. In the following, initial applications of this promising approach in two scenarios of significant clinical interest, that for noninvasive glucose measurements and for monitoring regenerative treatments of the heart, as well as initial *in vivo* demonstration, are discussed.

9.8 Initial Biomedical Applications

9.8.1 Noninvasive glucose measurement in tissue-like turbid media

Diabetes Mellitus is a chronic systemic disease, with no known cure, in which the body either fails to produce, or fails to properly respond to the glucose regulator hormone insulin. The most reliable current method for glucose monitoring in diabetic patients necessitates the drawing of blood, usually by a finger prick several times a day – a painful, inconvenient, and poorly compliant procedure. A tremendous need therefore exists for a *noninvasive* glucose monitoring method, as it would increase the determination frequency and enable better insulin and caloric intake, leading to a tighter glucose level control and preventing or delaying long-term complications. A variety of optical methods have been attempted for blood glucose monitoring including, near-infrared (NIR) spectroscopy, Raman spectroscopy, fluorescence, photoacoustics, optical coherence tomography and polarimetry, but none have shown the requisite sensitivity/specificity/accuracy [9]. Polarimetry, based on the chiral (handed) nature of the glucose molecules and their associated optical activity, is particularly promising as it is potentially specific to glucose. In fact, such measurements in clear media have been used for decades in the sugar industry. However, in a complex turbid medium like tissue, polarimetric attempts for glucose quantification have been confounded by several factors. One of the major stumbling blocks is that the optical rotation due to chiral substances in a turbid medium is swamped by the much larger changes in the orientation angle of the polarization vector due to scattering [10, 14, 18, 21].

It is thus essential to isolate the optical rotation caused exclusively by chiral molecules from the (often much larger) apparent rotation caused by the scattering / detection geometry effects. The matrix decomposition methodology is indeed able to perform this task, as shown in Figure 9.9 [30]. The variation of scattering induced rotation α is displayed as a function of distance from the point of illumination of a chiral ($\chi = 0.082^\circ$ cm^{-1}, corresponding to 100 mM concentration of glucose), nonbirefringent ($\Delta n = 0$), turbid medium (μ_s = 30 cm^{-1}, g = 0.95, thickness = 1 cm). The incident light was 45° polarized (Stokes vector [1 0 1 0] ^{T}) and the rotation of the linear polarization vector (α) was calculated from the recorded Stokes parameters [I Q U V] of light exiting the sample through the backscattering plane (X-Y plane, $Z = 0$) as

$$\alpha = 0.5 \times \tan^{-1}(U/Q) \tag{9.41}$$

As seen, changes in the polarization caused by scattering can manifest themselves as large apparent optical rotation. Decomposition analysis revealed that the large scattering-induced apparent rotation is due to linear diattenuation (also shown in the figure). This confounding effect is due mainly to the singly (weakly) backscattered photons and gradually decreases away from the exact backscattering direction [18] (see Section 9.7). Decomposition of the Mueller matrix can thus decouple this chirality-unrelated rotation from the much smaller ψ rotation values caused by the

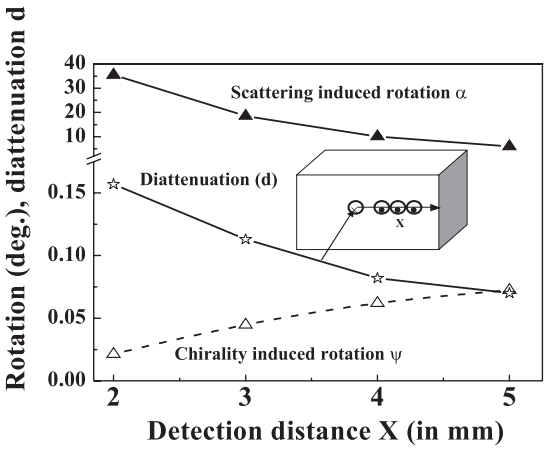

FIGURE 9.9: Calculated optical rotation ψ (derived from the decomposition of Monte Carlo-generated Mueller matrices, open triangles) of scattered light emerging in the backscattering direction as a function of distance from the center of the incident beam from a chiral (χ = 0.082° / cm, corresponding to 100 mM concentration of glucose) isotropic turbid medium (μ_s = 30 cm^{-1}, $g = 0.95$, thickness $t = 1$ cm). The corresponding scattering-induced rotation of the polarization vector derived from the Stokes parameters of scattered light (for incident Stokes vector [1 0 1 0] ^{T}) is shown by solid triangles. The scattering-induced diattenuation d is also shown. The inset shows the backwards detection geometry. The chirality-induced rotation approaches zero in the exact backscattering direction ($X = 0$, data not shown). (Adopted from [30]).

circular birefringence of the medium (which can then be linked to glucose concentration).

The ability to decouple the small optical rotation caused exclusively by chiral molecules even in the presence of numerous complexities due to the scattering/detection geometry and simultaneously occurring polarization effects bodes well for the potential application of this method for noninvasive glucose measurements in tissue. However, this remains to be rigorously investigated. In combination with Monte Carlo-determined path length distributions [32], we are currently exploring methods for extracting chiral molecule concentrations from derived optical rotations. Spectroscopic-based polarimetry combined with chemometric regression analysis is also being investigated to isolate the rotation due to glucose from that caused by other chiral biological constituents [33].

9.8.2 Monitoring regenerative treatments of the heart

The Mueller matrix decomposition method was explored for polarimetric monitoring of myocardial tissue regeneration following stem-cell therapy. The anisotropic organized nature of myocardial tissues stemming from their fibrous structure leads to linear birefringence. After suffering an infarction (heart attack), a portion of the myocardium is deprived of oxygenated blood and subsequently cardiomyocytes die, being replaced by the fibrotic (scar) tissue [34].

Recently, stem-cell-based regenerative treatments for myocardial infarction have been shown to reverse these trends by increasing the muscular and decreasing the scar tissue components [35]. These remodeling processes are expected to affect tissue structural anisotropy, and measurement of linear birefringence may offer a sensitive probe into the state of the myocardium after infarction and report on the success of regenerative treatments. However, these small birefringence alterations must be decoupled from the other confounding polarization effects that are present in the composite

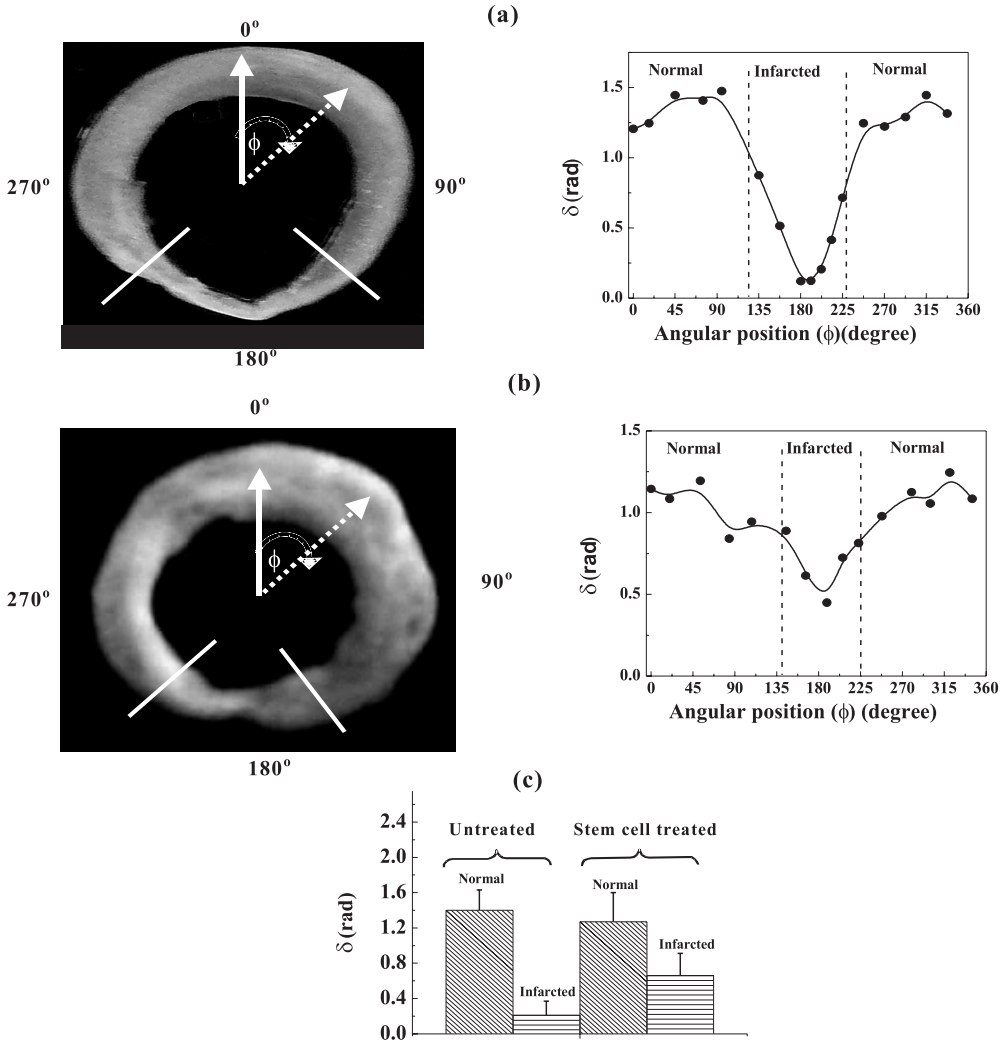

FIGURE 9.10: Linear retardance δ derived from transmission polarization measurements in 1-mm-thick sections from Lewis rat hearts following myocardial infarction. (a) Untreated tissues at four weeks following infarction, (b) tissues following stem-cell treatments, at four weeks following infarction, then two weeks after stem-cell therapy. The marked sector around $\varphi = 180^{\circ}$ indicates the infracted region. Symbols are experimentally derived values, and lines are a guide for the eye. Decreased birefringence levels in the infarcted region compared to normal regions are seen; this difference is reduced following stem-cell therapy, as infracted region retardance values increase towards normal-tissue levels. The results from birefringence measurements from the controls and the stem-cell treated groups of infracted hearts are shown in histogram form in (c). Error bars represent the standard deviation. Both untreated and stem-cell treated groups were comprised of 4 hearts, and 5 measurements were preformed in each region (normal and infarcted). (Adopted from [30]).

signals of the measured Mueller matrix elements from tissue.

Mueller matrices were recorded in the transmission geometry, from 1-mm thick *ex vivo* myocardial samples from Lewis rats after myocardial infarction, both with and without stem-cell treatments [30]. These were analyzed via polar decomposition to obtain linear retardance (δ) values. The δ values for two representative myocardial samples are shown in Figure 9.10.

The normal regions of the myocardium exhibit high levels of anisotropy, with derived δ values in the range of ~ 1.25 rad. A large decrease in linear retardance is seen in the infarcted region ($\delta \sim 0.2$ rad) of the untreated myocardium (Figure 9.10a). This arises because the native well-ordered anisotropic myocardium is replaced with disorganized isotropic scar tissue, likely collagenous in nature. An increase in δ towards the native levels is seen in the infarcted region after stem-cell treatment (Figure 9.10b). The bar graph of Figure 9.10c shows the mean linear retardance values from measurements of treated and untreated heart groups in the infarcted and normal regions. Statistically-significant ($p < 0.05$) differences in derived retardance values were obtained between normal and infarcted regions, and between infarcted regions with and without stem-cell treatments. An increase in retardance seen in the infarcted regions of the treated hearts indicates reorganization and re-growth (this was confirmed by histologic examination and is currently being corroborated by second harmonic generation microscopy for collagen imaging). These results show promise for the use of polarized light monitoring of stem-cell-based treatments of myocardial infarction, and current work is directed towards extending this novel method for *in vivo* biomedical deployment.

9.8.3 Proof-of-principle *in vivo* biomedical deployment of the method

The first *in vivo* use of the Mueller matrix decomposition method for tissue characterization was demonstrated using a dorsal skinfold window chamber mouse model [36]. In this model, the skin layer of an athymic nude mouse (NCRNU-M, Taconic) was removed from a 10 mm diameter region on the dorsal surface, and a titanium saddle was sutured in place to hold the skin flap vertically [37]. A protective glass coverslip (145 ± 15 μm thick) was placed over the exposed tissue plane. This allows for direct optical transmission measurements of polarized light through the ~ 500 μm thick layer. This model enables accurate measurements in an *in vivo* setting, free of many of the challenges inherent in examining fully 3D tissue structures.

Collagenase was injected into a region of dermal tissue to alter the structure of the extracellular matrix. The Mueller matrices were recorded both from the region of collagenase injection and a distant control region. Measurements were made before collagenase treatment and for 5 h postinjection at 30-min intervals, with an additional measurement at 24 h. Photographs of the dorsal skin flap window chamber model and of the experimental system, showing the mouse with its implanted window chamber in the path of the interrogating beam, are displayed in Figure 9.11.

Values for linear retardance (δ), net depolarization coefficient (Δ), optical rotation (ψ) and diattenuation (d) were extracted from the experimentally-derived Mueller matrices at each time point, using the polar decomposition approach [36]. The derived variations of δ and Δ (in both collagenase-treated and control regions) are shown as a function of time following collagenase injection, in Figure 9.12a and 9.12b respectively. Values for optical rotation ψ and diattenuation d did not change appreciably with treatment (data not shown). The value for δ is seen to vary from $\delta \approx 1.2$ rad to $\delta \approx 0.3$ rad in the treated region, in contrast to the control region where the values remain essentially constant at $\delta \approx 1$ rad. The decrease in birefringence is likely due to denaturation of the collagen fibers (collagenase cleaves the collagen fibers by breaking the peptide bonds connecting the monomer peptide units), which reduces the structural anisotropy. This was further confirmed by histology, where a reduction in collagen fibers was observed in the treatment region [36]. Using the approximate light path length, $l \approx 500$ μm (the true path length will be somewhat longer due to scattering [32]), the intrinsic birefringence Δn values were estimated as $\Delta n = \delta\lambda/2\pi l$, where $\lambda = 632.8$ nm. The birefringence values prior to treatment were calculated as $\Delta n \approx 2.2 \times 10^{-4}$, decreasing to $\Delta n \approx 0.6 \times 10^{-4}$, after treatment. These birefringence levels are reasonably close to

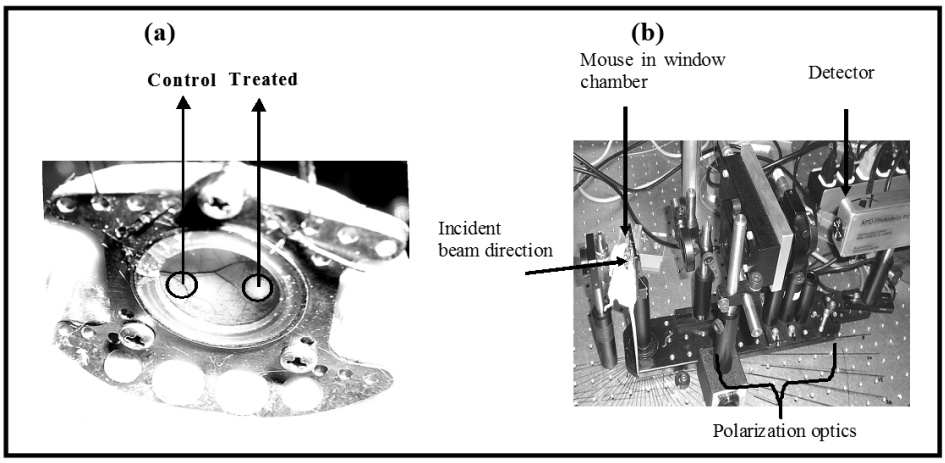

FIGURE 9.11: (a) Photograph of the dorsal skin flap window chamber model in a mouse. Measurements were made in two regions (collagenase treated and control) through the window chamber. (b) Photograph of the experimental system, showing the mouse with its implanted window chamber in the path of the interrogating beam. (Adopted from [36]).

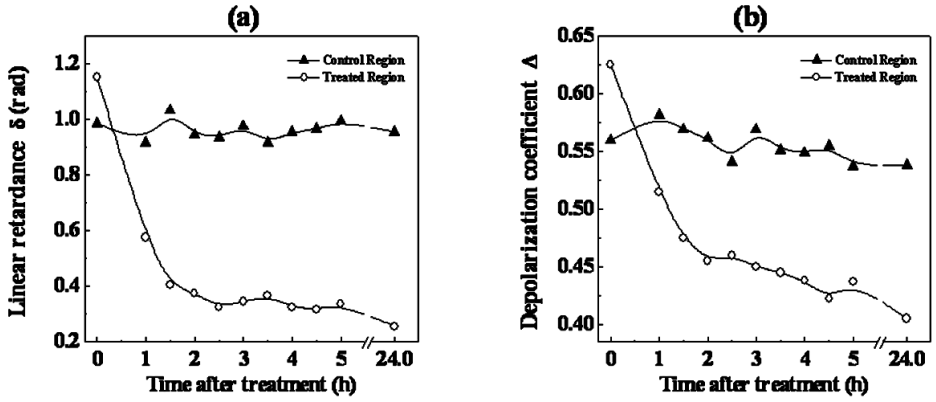

FIGURE 9.12: (a) Linear retardance δ and (b) net depolarization coefficient Δ before and as a function of time after collagenase injection in the treated and control regions. Symbols are experimentally derived values, and lines are a guide for the eye. (Adopted from [36]).

those found in the literature for tissue birefringence, typically $\sim 1 \times 10^{-3}$ [38].

In addition to the observed variation in δ, a decrease in the net depolarization coefficient Δ after treatment, from ~ 0.63 to ~ 0.45, was also noted in the treated region (Figure 9.11b). The values in the control region were again observed to remain essentially constant. This reduction in depolarization is also due to the destruction of the collagen fibers, since these represent one of the primary scattering structures in tissue [24]. Using the changes in the depolarizing properties of the tissue, the scattering coefficient of the tissue was determined using the polarization-sensitive Monte Carlo simulations. The values for μ_s were estimated to be 182 cm^{-1} for the pretreatment tissue and 134 cm^{-1} for the posttreatment tissue, which are in reasonable agreement with literature values [24]. These results demonstrate the ability of the method to quantify changes in tissue structure using polarized light *in vivo*. The interpretation of measured changes in values for birefringence and depolarization

show promise for the method's ability to accurately quantify biologically-relevant tissue parameters such as scattering and birefringence.

To conclude this section, the utility of the novel polar Mueller matrix decomposition approach has been initially explored in two important potential biomedical applications, for noninvasive glucose measurement in tissue-like turbid media and for quantification of tissue structural anisotropy. The initial *in vivo* use of the method for polarimetric tissue characterization has also been demonstrated. Results of these studies show promise and warrant further exploration. We are currently expanding our investigations for the use of this promising method *in vivo*, both for noninvasive measurements of glucose and for monitoring the response of infarcted myocardial tissues to stem-cell therapies.

9.9 Concluding Remarks on the Prospect of the Mueller Matrix Decomposition Method in Polarimetric Assessment of Biological Tissues

In this chapter, a novel general method for polarimetry analysis in turbid media based on polar Mueller matrix decomposition has been discussed. The ability of this approach for delineating individual intrinsic polarimetry characteristics in complex tissue-like turbid media was validated theoretically with a polarized-light Monte Carlo model, and experimentally with a polarization-modulation/synchronous detection setup on optical phantoms having controlled sample polarizing properties. The individual polarization effects can be successfully decoupled and quantified despite their simultaneous occurrence, even in the presence of the numerous complexities due to multiple scattering. The ability to isolate individual polarization properties provides a potentially valuable noninvasive tool for biological tissue characterization. Specifically, concentration determination of optically active molecules such as glucose and quantification of tissue structural anisotropy are two important biomedical avenues that have been initially explored. Clearly, there are many other potential applications in biomedicine, both in tissue diagnostics and in treatment response monitoring.

Acknowledgments

Research support from the Natural Sciences and Engineering Research Council of Canada (NSERC) and collaborations with Richard D.Weisel, Ren-Ke Li, Shu-hong Li, Eduardo H. Moriyama, and Brian C. Wilson are gratefully acknowledged. The authors are also thankful to Marika A. Wallenburg for her help during the preparation of the manuscript.

References

[1] V. Ronchi, *The Nature of Light*, Harvard University Press, Cambridge, Massachusetts (1970).

[2] J. Michl and E.W. Thulstrup, *Spectroscopy with Polarized Light*, Wiley-VCH, New York (1986).

[3] D.S. Kliger, J.W. Lewis, and C.E. Randall, *Polarized Light in Optics and Spectroscopy*, Academic Press–Harcourt Brace Jovanovich, New York (1990).

[4] L.V. Wang, G.L Coté, and S. L. Jacques, "Special section guest editorial: tissue polarimetry," *J. Biomed. Opt.* **7**, 278 (2002).

[5] V.V. Tuchin, L. Wang, and D. Zimnyakov, *Optical Polarization in Biomedical Applications*, Springer-Verlag, Berlin, Heidelberg, N.Y., (2006).

[6] V.V. Tuchin (ed.), *Handbook of Optical Sensing of Glucose in Biological Fluids and Tissues*, CRC Press, Taylor & Francis Group, London, (2009).

[7] P.J. Wu and J.T. Walsh Jr., "Stokes polarimetry imaging of rat tail tissue in a turbid medium: degree of linear polarization image maps using incident linearly polarized light," *J. Biomed. Opt.* **11**, 014031 (2006).

[8] J.F. de Boer and T.E. Milner, "Review of polarization sensitive optical coherence tomography and Stokes vector determination," *J. Biomed. Opt.* **7**, 359–371 (2002).

[9] R.J. Mc Nichols and G.L. Coté, "Optical glucose sensing in biological fluids: an overview," *J. Biomed. Opt.* **5**, 5–16 (2000).

[10] X. Guo, M.F.G. Wood, and I.A. Vitkin, "Angular measurement of light scattered by turbid chiral media using linear Stokes polarimeter," *J. Biomed. Opt.* **11**, 041105 (2006).

[11] D. Côte and I.A. Vitkin, "Balanced detection for low-noise precision polarimetric measurements of optically active, multiply scattering tissue phantoms," *J. Biomed. Opt.* **9**, 213–220 (2004).

[12] R.R. Ansari, S. Bockle, and L. Rovati, "New optical scheme for a polarimetric-based glucose sensor," *J. Biomed. Opt.* **9**, 103–115 (2004).

[13] I.A. Vitkin, R.D. Laszlo, and C.L. Whyman, "Effects of molecular asymmetry of optically active molecules on the polarization properties of multiply scattered light," *Opt. Express* **10**, 222–229 (2002).

[14] D. Côté and I.A. Vitkin, "Robust concentration determination of optically active molecules in turbid media with validated three-dimensional polarization sensitive Monte Carlo calculations," *Opt. Express* **13**, 148–163 (2005).

[15] R.A. Chipman, "Polarimetry," Chap. 22 in *Handbook of Optics*, 2nd ed., M. Bass, Ed., Vol. **2**, pp. 22.1–22.37, McGraw-Hill, New York (1994).

[16] C. Brosseau, *Fundamentals of Polarized Light: A Statistical Optics Approach*, Wiley, New York (1998).

[17] N. Ghosh, M.F.G. Wood, and I.A. Vitkin, "Mueller matrix decomposition for extraction of individual polarization parameters from complex turbid media exhibiting multiple scattering, optical activity and linear birefringence," *J. Biomed. Opt.* **13**, 044036 (2008).

[18] N. Ghosh, M.F.G. Wood, and I.A. Vitkin, "Polarimetry in turbid, birefringent, optically active media: a Monte Carlo study of Mueller matrix decomposition in the backscattering geometry," *J. Appl. Phys.* **105**, 102023 (2009).

[19] S. Yau Lu and R.A. Chipman, "Interpretation of Mueller matrices based on polar decomposition," *J. Opt. Soc. Am. A* **13**, 1106–1113 (1996).

[20] M.F.G. Wood, X. Guo, and I.A. Vitkin, "Polarized light propagation in multiply scattering media exhibiting both linear birefringence and optical activity: Monte Carlo model and experimental methodology," *J. Biomed. Opt.* **12**, 014029 (2007).

[21] S. Manhas, M.K. Swami, P. Buddhiwant, N. Ghosh, P.K. Gupta, and K. Singh,"Mueller matrix approach for determination of optical rotation in chiral turbid media in backscattering geometry," *Opt. Express* **14**, 190–202 (2006).

[22] J. Morio and F. Goudail, "Influence of the order of diattenuator, retarder, and polarizer in polar decomposition of Mueller matrices," *Opt. Lett.* **29**, 2234–2236 (2004).

[23] R. Ossikovski, A. De Martino, and S. Guyot, "Forward and reverse product decompositions of depolarizing Mueller matrices," *Opt. Lett*. **32**, 689 (2007).

[24] A.J. Welch and M.J.C. van Gemert, *Optical-Thermal Response of Laser Irradiated Tissue,* Plenum Press, New York (1995).

[25] L. Wang, S.L. Jacques and L. Zheng, "MCML-Monte Carlo modeling of light transport in multi-layered tissues," *Comput. Methods Programs Biomed.* **47**, 131–146 (1995).

[26] M. Moscoso, J.B. Keller, and G. Papanicolaou, "Depolarization and blurring of optical images by biological tissues," *J. Opt. Soc. Am. A* **18**, 949–960 (2001).

[27] D. Côté and I.A. Vitkin, "Pol-MC: a three dimensional polarization sensitive Monte Carlo implementation for light propagation in tissue," available online at http://www.novajo.ca/ont-canc-instbiophotonics/.

[28] C. F. Bohren and D.R. Huffman, *Absorption and Scattering of Light by Small Particles*, Chap. 2, Wiley, New York (1983).

[29] R. Clark Jones, "New calculus for the treatment of optical systems VII. Properties of the N-matrices," *J. Opt. Soc. Am.* **38**, 671–685 (1948).

[30] N. Ghosh, M.F.G. Wood, S.H. Li, R.D. Weisel, B.C. Wilson, Ren-Ke Li, and I.A. Vitkin, "Mueller matrix decomposition for polarized light assessment of biological tissues," *J. Biophotonics* **2** (3), 145–156 (2009).

[31] N. Ghosh, M.F.G. Wood, M.A. Wallenberg and I.A. Vitkin, "Influence of the order of the basis matrices on the Mueller matrix decomposition-derived polarization parameters in complex tissue-like turbid media," *Opt. Commun*. (in press).

[32] X. Guo, M.F.G. Wood, and I.A. Vitkin, "Monte Carlo study of path length distribution of polarized light in turbid media," *Opt. Express* **15**, 1348–1360 (2007).

[33] M.F.G. Wood, D. Côté, and I.A. Vitkin, "Combined optical intensity and polarization methodology for analyte concentration determination in simulated optically clear and turbid biological media," *J. Biomed. Opt.* **13**, 044037 (2008).

[34] Y. Sun, J.Q. Zhang, J. Zhang, and S. Lamparter, "Cardiac remodeling by fibrous tissue after infarction," *J. Lab. Clin. Med.* **135**, 316–323 (2000).

[35] D. Orlic, et al., "Bone marrow cells regenerate infarcted myocardium," *Nature* **410**, 701–705 (2001).

[36] M.F.G. Wood. N. Ghosh, E.H. Moriyama, B.C. Wilson, and I.A. Vitkin, "Proof-of-principle demonstration of a Mueller matrix decomposition method for polarized light tissue characterization *in vivo,*" *J. Biomed. Opt.* **14**, 014029 (2009).

[37] M. Khurana, E.H. Moriyama, A. Mariampillai, and B.C. Wilson, "Intravital high-resolution optical imaging of individual vessel response to photodynamic treatment," *J. Biomed. Opt.* **13**, 040502 (2008).

[38] W. Wang and L.V. Wang, "Propagation of polarized light in birefringent media: a Monte Carlo study," *J. Biomed. Opt.* **7**, 350–358 (2002).